3D printed patient-specific fixation plates for the treatment of slipped capital femoral epiphysis

Topology optimization vs. conventional design

Moosabeiki, V.; de Winter, N.; Cruz Saldivar, M.; Leeflang, M. A.; Witbreuk, M. M.E.H.; Lagerburg, V.; Mirzaali, M. J.; Zadpoor, A. A.

DOI
10.1016/j.jmbbm.2023.106173

Publication date
2023

Document Version
Final published version

Published in
Journal of the mechanical behavior of biomedical materials

journal of the mechanical behavior of biomedical materials 148 (2023) 106173

Contents lists available at ScienceDirect

Journal of the Mechanical Behavior of Biomedical Materials

journal homepage: www.elsevier.com/locate/jmbbm

3D printed patient-specific fixation plates for the treatment of slipped capital femoral epiphysis: Topology optimization *vs.* conventional design

V. Moosabeiki [a,*], N. de Winter [a,c], M. Cruz Saldivar [a], M.A. Leeflang [a], M.M.E.H. Witbreuk [b], V. Lagerburg [c], M.J. Mirzaali [a], A.A. Zadpoor [a,d]

[a] *Department of Biomechanical Engineering, Faculty of Mechanical, Maritime, and Materials Engineering, Delft University of Technology (TU Delft), Mekelweg 2, 2628, CD, Delft, the Netherlands*
[b] *Department of Orthopaedic Surgery, OLVG, Oosterpark 9, 1091, AC, Amsterdam, the Netherlands*
[c] *Medical Physics, OLVG, Oosterpark 9, 1091, AC, Amsterdam, the Netherlands*
[d] *Department of Orthopedic Surgery, Leiden University Medical Center, Albinusdreef 2, 2333, ZA, Leiden, the Netherlands*

ARTICLE INFO

Keywords:
Orthopedic surgery
Patient-specific medical devices
Topology optimization
Finite element analysis
Biomechanical validation

ABSTRACT

Orthopedic plates are commonly used after osteotomies for temporary fixation of bones. Patient-specific plates have recently emerged as a promising fixation device. However, it is unclear how various strategies used for the design of such plates perform in comparison with each other. Here, we compare the biomechanical performance of 3D printed patient-specific bone plates designed using conventional computer-aided design (CAD) techniques with those designed with the help of topology optimization (TO) algorithms, focusing on cases involving slipped capital femoral epiphysis (SCFE). We established a biomechanical testing protocol to experimentally assess the performance of the designed plates while measuring the full-field strain using digital image correlation. We also created an experimentally validated finite element model to analyze the performance of the plates under physiologically relevant loading conditions. The results indicated that the TO construct exhibited higher ultimate load and biomechanical performance as compared to the CAD construct, suggesting that TO is a viable approach for the design of such patient-specific bone plates. The TO plate also distributed stress more evenly over the screws, likely resulting in more durable constructs and improved anatomical conformity while reducing the risk of screw and plate failure during cyclic loading. Although differences existed between finite element analysis and experimental testing, this study demonstrated that finite element modelling can be used as a reliable method for evaluating and optimizing plates for SCFE patients. In addition to enhancing the mechanical performance of patient-specific fixation plates, the utilization of TO in plate design may also improve the surgical outcome and decrease the recovery time by reducing the plate and incision sizes.

1. Introduction

Slipped capital femoral epiphysis (SCFE) is a prevalent hip disorder in adolescents, where the growth plate, also known as physis, is disrupted and the metaphysis, the part of the bone located next to the growth plate, displaces in a posterior-inferior direction with respect to the capital femoral epiphysis (*i.e.,* femoral head) (Manoff et al., 2005; Novais and Millis, 2012). Obesity, endocrine disorders, oblique physeal growth, and increased femoral retroversion increase the risk of SCFE due to either a weakening (endocrine) of the growth plate or an increased mechanical stress on the growth plate (Perry et al., 2018; Herngren et al., 2017; Wylie and Novais, 2019).

In situ pinning is the first step in preventing SCFE progression in mild cases. However, it has been linked to osteoarthritis later in life and does not restore normal anatomy or relieve pain, particularly in severe SCFE cases (Wylie and Novais, 2019). Corrective osteotomy surgery, commonly intertrochanteric osteotomy, is performed on patients with moderate SCFE. The proximal femur (*i.e.,* femur head) and femur shaft are realigned with a femoral head–neck osteotomy, then stabilized using a fixation plate (Aronsson et al., 2006; Witbreuk et al., 2009). Intertrochanteric osteotomy restores hip motion and biomechanics while reducing the risk of avascular necrosis (Loder et al., 2000). The surgery is considered successful when the mobility and pain level of the patient improve and no plate or screw failure occurs. The bone is expected to

* Corresponding author.
E-mail address: v.moosabeiki@tudelft.nl (V. Moosabeiki).

https://doi.org/10.1016/j.jmbbm.2023.106173
Received 3 July 2023; Received in revised form 5 October 2023; Accepted 9 October 2023
Available online 11 October 2023

have adequately healed in six weeks, allowing for gradual hip loading. One year after the surgery, the plate is usually removed as it is no longer required for bone stability (Ma et al., 2017; Erickson et al., 2017). However, reports indicate that plate failures do occur with 12.5% of these failures reported within the first six weeks (Henderson et al., 2011), with most plate failures occurring between three to six months post-surgery (Henderson et al., 2011; Shibahara et al., 2002; Gutwald et al., 2017). These late failures are usually related to non-union of the bone after surgery.

In the field of orthopedic surgery, temporary fixation of bones following osteotomy is achieved using commercially available plates of standard size, which are bent to fit the bones as closely as possible. However, standard plates are not always suitable for complex cases, and a mismatch between the plate and bone can increase the risk of failure after surgery (Fan et al., 2018; Chen et al., 2017; Dobbe et al., 2013; Brouwer de Koning et al., 2023). Patient-specific plates offer a better anatomical fit and reduce the risk of plate failure. These plates can be designed using virtual surgical planning tools and computationally enabled design methods, such as finite element analysis (FEA) and topology optimization (TO) (Zadpoor, 2017; Van Kootwijk et al., 2022; Chen et al., 2018; Wu et al., 2021; Mirzaali et al., 2022; van Kootwijk et al., 2023), to optimize their shape, topology, and geometry, thereby limiting the incision size, minimizing the risk of infection, and promoting bone healing (Wang et al., 2017; Arnone et al., 2013; Mirzaali et al., 2019, 2021, 2023). However, a smaller plate may also result in lower stiffness and decreased stability, compromising its effectiveness in supporting the affected area (Wang et al., 2017; Arnone et al., 2013). A workflow that combines design optimization and computational/experimental testing is, therefore, required to facilitate the integration of patient-specific plates into routine medical practice.

Despite some studies reporting the design workflow for patient-specific femur fixation plates, there is a lack of research into their biomechanical performance under physiological loading conditions (Al-Tamimi et al., 2020). Moreover, while the mechanical properties of non-customized fixation plates have been studied, there is limited research into patient-specific bone plates for femur fixation and the optimal parameters for efficient and stable fracture fixation (Arnone et al., 2013; Stoffel et al., 2003).

In this study, we aimed to improve the biomechanical performance of a patient-specific proximal femur fixation plate through the incorporation of computational modelling and TO into the design process. Our objective was to optimize the plate size and enhance its biomechanical performance while maintaining its elastic stiffness. To accomplish this, we designed both above-mentioned types of fixation plates, manufactured them using 3D printing, and subjected them to mechanical loads while measuring the full-field strain patterns using digital image correlation. We also developed an experimentally validated FE model to evaluate the plates under two physiological loading conditions: two-leg stance (with a maximum reaction force of 1 time body weight (BW) and walking (with a maximum reaction force of 3 times BW). Our FE model considered a scenario in which bone healing is delayed, but gradual load bearing has already started, with a focus on the worst-case scenario of walking. The ultimate goal was to assist clinical engineers in designing more reliable and optimally sized patient-specific plates for the treatment of SCFE defects.

2. Materials and methods

A 13-year-old male patient with a body weight of 100 kg was referred to the OLVG Hospital (Amsterdam, the Netherlands) for the corrective osteotomy of the left proximal femur affected by SCFE (see Ethical Approval). A patient-specific CAD plate had been designed and utilized during surgery at OLVG. Here, we perform a retrospective study in which an alternative fixation plate is designed and compared with the actual implant in a laboratory setting. The workflow for creating a patient-specific bone plate using both conventional CAD techniques and TO is outlined in Fig. 1. It starts with image acquisition and clinical diagnosis (Fig. 1a–i). The 3D bone model is then generated from segmented CT images (Fig. 1a-ii–iii). Consequently, virtual proximal femur osteotomies are performed (Fig. 1b) and screw positions are defined (Fig. 1c–i). Finally, a biomechanical engineer can design the patient-specific plate using computational tools, such as FEA software and TO (Fig. 1c) or CAD software (Fig. 1d).

2.1. Image segmentation and virtual reconstruction

Image acquisition was performed using a Revolution™ CT scanner (GE Healthcare, Milwaukee, WI, USA) at a tube voltage of 100 kVp, a current of 132 mA, and a slice thickness of 1.5 mm. Image segmentation and 3D model generation of the femur bone were done using Materialise Mimics® 21.0 (Materialise, Belgium) (Fig. 1a-ii–iii). Foreground-background segmentation was applied with an optimal threshold of 226–3071 Hounsfield units (HU) to generate the 3D model of the femur. The CT images revealed a single pin with a high HU value in the proximal head of the femur, which had been placed to prevent further femoral head slippage. This pin was excluded from the 3D model as it was removed during the corrective surgery. The 3D bone model was then exported to 3-matic® 13.0 (Materialise, Belgium) for virtual reconstruction of the corrective osteotomy and plate design (Fig. 1b–i).

The main objective of surgical treatment for SCFE is to realign the femoral head relative to the acetabulum and to secure stable fixation of proximal part of the femur, which requires at least 50% of the osteotomy to be in contact with each other to facilitate healing of the osteotomy. In virtual planning, the desired position of the femoral head can be determined based on the healthy opposite femur of the same patient, or, if both femurs are affected and cannot serve as a reference (as was the case in this study), the healthy femur of another patient can be used, in consultation with an orthopedic surgeon (Aronsson et al., 2006; Loder et al., 2000). A planar cut was first made between the lesser trochanter and the femoral neck (Fig. 1b–ii). Next, the shaft and femoral head were rotated along the sagittal, axial, and coronal planes to obtain acceptable hip angles (Fig. 1b-iii–v). The overlap between the femoral head and shaft was then cut (Fig. 1b-vi–vii), and the wedge-shaped excess part was removed (Fig. 1b–viii) to form the corrected femur model (Fig. 1b–ix). The accuracy of the angles in the final model was confirmed by re-importing it into Materialise Mimics® and overlaying it on the CT images (Fig. 1a–i).

2.2. Synthetic bone

We used a fused deposition modelling (FDM) 3D printer (Ultimaker S5, Ultimaker B.V., The Netherlands) and poly-lactic acid (PLA) filaments (Ultimaker PLA-white, 750 g Natural with a filament diameter of 2.85 mm) to additively manufacture a model of the SCFE-affected femur. We divided the 3D bone model into two sections, namely the compact and porous regions, and segmented the CT images to identify the areas whose grey values were indicative of cortical ($>$ 226 HU) and cancellous bone ($<$ 226 HU). These regions were then imported into the Ultimaker Cura software (V4.9.0) and were 3D printed using the printing parameters listed in Table S1 of the supplementary document.

2.3. Computational modelling

The finite element modelling and topology optimization in this study were performed using the commercial software suite Abaqus/CAE 2017 (Simulia, Dassault Systemes, France). First, we created a simplified model to replicate the experimental conditions (Figs. 2a and 3a–b). This model was then extended to include a musculoskeletal system and simulate more complex physiological loading conditions, such as two-leg stance and walking (Fig. 3c). Next, we analyzed CAD plate designs featuring various screw positions, initially selected by the surgeon, under walking loading condition to establish the design domain for

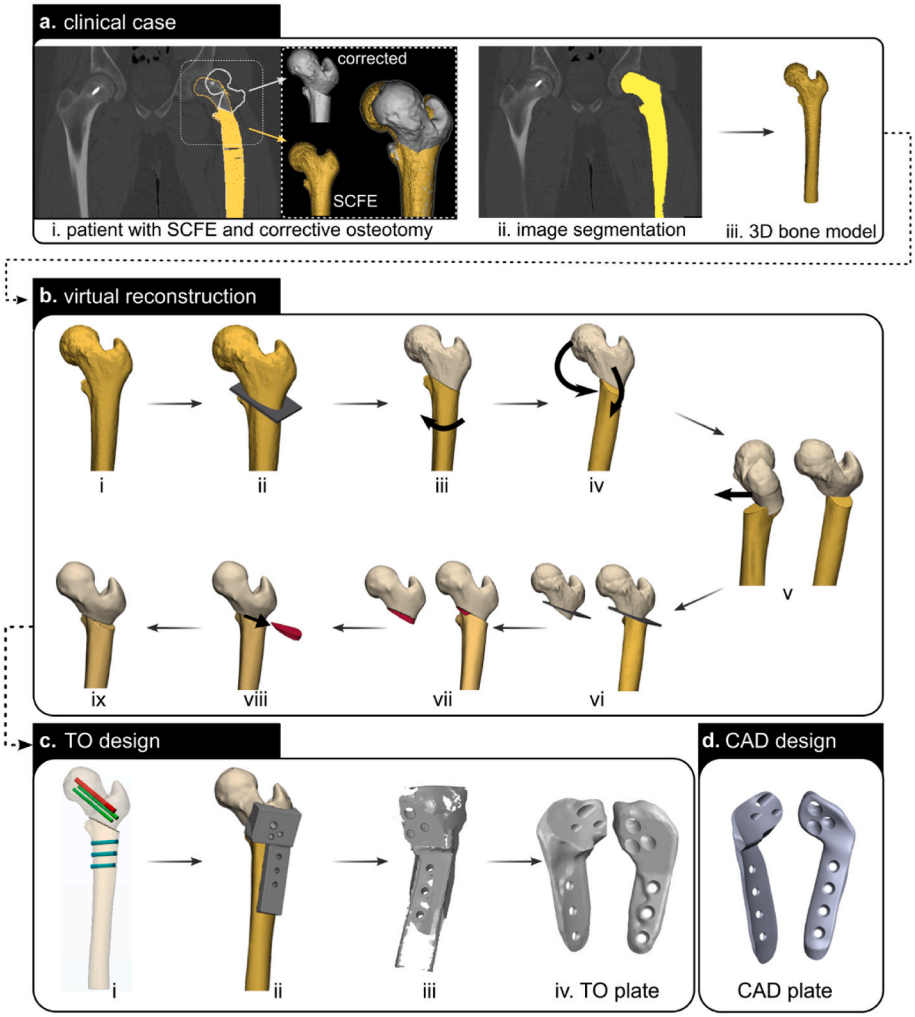

Fig. 1. The workflow used for the design of a topology-optimized proximal femur fixation plate for the treatment of SCFE patients. The process starts with image acquisition and clinical diagnosis (a–i) followed by image segmentation (a-ii) and the generation of a 3D model of the affected bone (a-iii). The virtual reconstruction of the corrective osteotomy is carried out by cutting the bone along a plane placed between the femoral head and lesser trochanter (b-ii), rotating the bone shaft for physiological endo/exo rotation (b-iii), adjusting the rotation of the proximal part of the femur in the coronal and sagittal planes (b-iv), and translating it for proper placement in the acetabulum (b–v). The removal of the overlap between the proximal femur and shaft is achieved by creating a plane (b-vi), cutting the proximal femur (b-vii), removing the wedge (b-viii), and transferring the corrected bone model to the plate design stage (b-ix). The screw positions are defined (c–i) and the initial design area is placed on the bone after subtracting the bone surface (c-ii). The outcome of the topology optimization process (c-iii) is post-processed to produce the final product (c-iv). The design of the CAD plate used in this study is presented in subfigure (d).

topology optimization (Fig. 4a). The screw positions were altered in four configurations, including P3-D4 (three screws proximally in the head and four screws distally in the shaft) (Fig. 4a–i), P3-D3 (Fig. 4a–ii), P3-D2 (Fig. 4a–iii), and P2-D4 (Fig. 4a–iv). The design area was defined based on the screw configuration P3-D3 (Figure S1c) and was optimized to withstand the extreme loading conditions in this study, which was walking. A von Mises stress limit of 435 MPa (*i.e.,* a 50% safety margin from the yield strength of Ti–6Al–4V) was considered to be the maximum safe stress. The validity of the FE model was established by comparing its predictions with experimental data obtained using digital image correlation (DIC) for CAD plates (Fig. 2c and the supplementary movie S1).

2.3.1. Material assignment

We discretized the surfaces of the model with a maximum element edge length of 1.8 mm and generated the volume meshes with a maximum element edge length of 2.2 mm using 4-node tetrahedral (C3D4) elements (as illustrated in Fig. 3a). Isotropic linear elastic material models were used for all the materials.

In the FE analysis of the experimental loading conditions, the material properties of PLA were assigned homogenously to the synthetic femur model. It has been reported that the elastic modulus (E) of 3D printed compact PLA can vary between 350 and 3500 MPa (Farah et al., 2016). However, the mechanical properties of 3D printed PLA are very consistent as long as the filament batch, printing machine, and printing parameters are kept the same (Anderson, 2017). The variations in the mechanical properties of PLA are influenced by multiple factors, including manufacturing processes, material composition, and testing conditions. Additionally, its Poisson's ratio (ν) is recorded at 0.36, and its density (ρ) is $\sim$ 1240 kg/m^3 (Farah et al., 2016). The material properties were then assigned based on the grey values obtained from CT images. The higher grey values ($>$ 226 HU) corresponded to an average value of $E = 350$ MPa and $\rho = 1240$ kg/m^3, representing the cortical bone. The lower grey values ($<$ 226 HU) corresponded to $E = 140$ MPa and $\rho = 496$ kg/m^3, representing the cancellous bone (Fig. 3b).

To evaluate the performance of the plates under physiological loading conditions, we introduced the mechanical properties of the femur into the physiologically based FE model, using a grey-value-based approach. This method enabled us to model the effects of physiological loading conditions on the femur accurately, with a total of 15 material

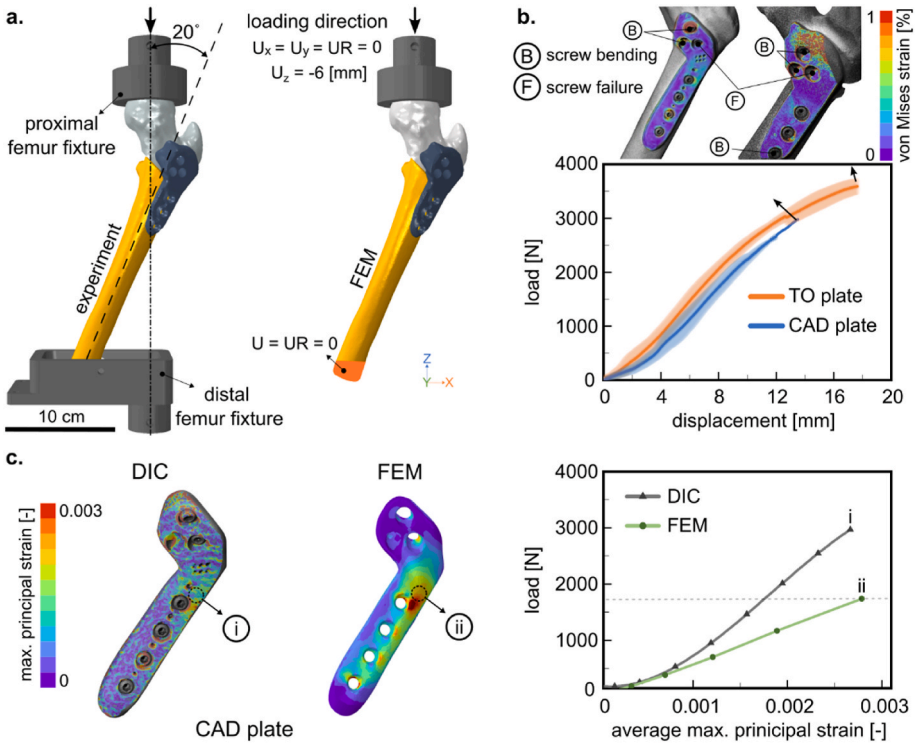

Fig. 2. (a) The experimental setup (left) and displacement (U) and rotation (UR) constraints in the finite element model (right). (b) The force-displacement curves obtained from the quasi-static compression tests for the CAD and TO plates and the true effective (von Mises) strain fields of the plates prior to failure, measured by DIC. (c) A comparison between the true maximum principal strain values measured by DIC and the FEA-predicted values of the logarithmic (LE) maximum principal strain within the linear elastic region of the CAD plate (up to 1700 N).

properties ranging between 14.2 and 19199.2 MPa for the Young's modulus (E) and 50–1573.1 kg/m^3 for density (ρ) (Fig. 3b). We assigned a homogeneous material value of $\rho = 50$ kg/m^3 to all the negative HU-values up to 100 HU. To cover the HU values between 101 and 1840 HU, we used 14 materials ranging between $\rho_{min} = 107$ and $\rho_{max} = 1568$ Kg/m^3. The material properties were calculated using the empirical expressions (*i.e.,* $= 0.004\rho^{2.09}$) and $\nu = 0.3$ (Ciarelli et al., 1991). The proximal part of the femur required an additional material, as the CT scan included a pin in the proximal femur with a very high HU value. We assigned low mechanical properties (*i.e.,* $E = 14.2$ MPa and $\rho =$ 50 kg/m^3) to this area, since the pin was not included in our model. The following mechanical properties were assigned to the Ti–6Al–4V plates: $E = 110$ GPa, and $\nu = 0.3$ (Sathish et al., 2020; Soni and Singh, 2020; Chung, 2018). The yield strength (S_{Yield}) of the 3D-printed titanium alloy plates was considered to be 870 MPa (Kobryn and Semiatin, 2001).

2.3.2. Loads and boundary conditions

In the FE model, we imported the proximal femur fixture as an undeformable rigid object into the model to apply the load on the proximal femur head and distally fixated all the 6°-of-freedom of the shaft (U = UR = 0) to represent the experimental setup (Fig. 2a). The load was applied by displacing the fixture 6 mm inferiorly (*i.e.,* in the negative z-direction in Fig. 2a), which was sufficient to capture the linear portion of the load-displacement curve obtained from the biomechanical experiments. Since the joint contact force on the femur is applied at a physiologically relevant angle, the bone-plate construct was rotated 3° around the x-axis (*i.e.,* flexion), 20° around the y-axis (*i.e.,* adduction), and −43.6° around the z-axis (Simoes et al., 2000). A friction coefficient of 0.3 (Aziz et al., 2020) was assigned to the interfaces between the PLA parts (*i.e.,* shaft and the head) and the head and fixture, while a friction coefficient of 0.45 was assigned to model the contact between the synthetic bone and the plate (Yu et al., 2005; Zhiani Hervan et al., 2021).

To assess the plates under physiological loading conditions, we considered joint reaction force and the major muscle groups, specifically the abductor forces on the greater trochanter, and the iliopsoas on the lesser trochanter (Taylor et al., 1996; Cheal et al., 1992; Reina-Romo et al., 2014). During corrective surgery, the vastus lateralis, one of the most dominant quadriceps muscles, was detached and then reattached, leading to significant weakening and decreased load on the proximal femur. The decision to exclude it from the computational model was made in consultation with the surgeon. However, the muscles acting on the lesser and greater trochanters were stretched, not negatively affected, and were, thus, included in the model.

To minimize the bending moments and achieve uniform stress distribution within the bone, the FEA model incorporated a joint contact force with an inclination angle of 20° with respect to the vertical direction (Fig. 3c). This angle remains constant throughout the stance phase of the gait cycle, while supporting the maximum load during walking (Bergmann et al., 2016). The physiological model necessitated adjustments to the interactions and constrains. Loading areas of 180–300 mm^2 were designated for joint reaction forces, abductor, and iliopsoas in accordance with literature and muscle attachment sites (Fan et al., 2018; MacLeod et al., 2018; Yang et al., 2020). A friction coefficient of 0.45 was used at the contact interface between the femoral head and the shaft (Von Fraunhofer et al., 1985; Tilton et al., 2020; Shockey et al., 1985), while a penalty friction coefficient of 0.4 was utilized to model the interaction between the femur and Ti–6Al–4V plate (Fan et al., 2018; Yu et al., 2005; Cordey et al., 2000; Pendergast and Rusovici, 2015). The distal surface of the femur was completely restricted from translation (Fig. 3c) (Arnone et al., 2013; Nobari et al., 2010; Peleg et al., 2006). Non-locking screws were used in both experiments and were simulated in the computational models. To simulate such screws, two reference points were defined: one at the middle of the hole in the plate and another at the bottom part of the hole within the bone. These reference points were kinematically coupled to the internal surfaces of

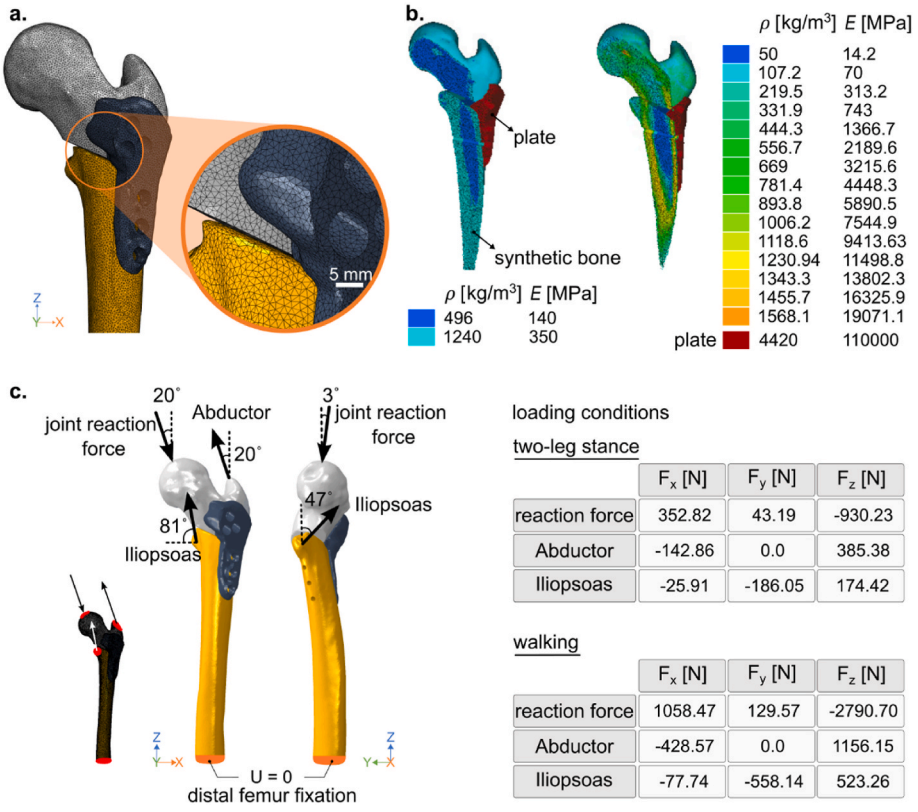

loading conditions

two-leg stance

	F_x [N]	F_y [N]	F_z [N]
reaction force	352.82	43.19	-930.23
Abductor	-142.86	0.0	385.38
Iliopsoas	-25.91	-186.05	174.42

walking

	F_x [N]	F_y [N]	F_z [N]
reaction force	1058.47	129.57	-2790.70
Abductor	-428.57	0.0	1156.15
Iliopsoas	-77.74	-558.14	523.26

Fig. 3. (a) Overview of surface mesh applied to bone and plate. (b) Cross-sectional views of material assignment to volume mesh of synthetic (PLA) bone (left) and patient's bone (right). The color scale represents the corresponding values of the density and Young's modulus calculated for bone and plate. (c) The constraints and muscle force directions for physiological loading conditions along with the muscle attachment regions (left) and the muscle forces in three directions during two-leg stance and walking (right).

each hole in the plate and in the bone cavity. This kinematic coupling condition restricted the movement between these reference points *(i.e.,* master) and their corresponding bone and plate surfaces (*i.e.,* slave) in all degrees of freedom. The two reference points were then linked together using a multi-point constraint (*i.e.,* beam) to represent the screw. Such a simulation approach reduces computational time by simplifying the interaction of the non-locking screw with its interfaces in the plate and bone (Figure S2 in the supplementary document). These constraints ensured that the components of the screw, bone, and plate components were appropriately connected and functioned as a unified system.

2.4. Plate design

We evaluated two different approaches for creating patient-specific femoral plates: computer-aided design (CAD plate) and topology optimization (TO plate). Our considerations for the TO plate were influenced by the previously designed CAD plate, which was successfully implanted in the patient. As a result, both approaches ensured that the plate size and shape were tailored to the patient's anatomy, making them effective for orthopedic plate design.

The CAD plate (Fig. 1d) was developed at the OLVG hospital in collaboration with the orthopedic surgeon using SolidWorks® 2020 (Dassault Systèmes SolidWorks Corporation). The custom plate was modelled after the shape of pediatric hip plates and was adapted to the patient's anatomy. The distal part of the plate had a thickness ranging between 3.6 and 4.3 mm, with the proximal part having a thickness of up to 14.0 mm. The distal width was approximately 20.0 mm (19.5–20.2 mm). The CAD plate used in this study was slightly different from the version used in clinical practice. The plate was designed with small holes, strategically positioned along the lateral-distal part of the plate, to serve as internal markers for the purpose of monitoring print quality (Fig. 2c). Three proximal and four distal cannulated dynamic compression screws (DePuy Synthes, West Chester, PA) were used to secure the plate to the bone. Six screws had a diameter of 4.5 mm, while the seventh (*i.e.*, the most proximal screw) had a diameter of 6.5 mm. The lengths of the screws varied between 32 and 38 mm distally and between 65 and 71 mm proximally. Further details regarding the CAD plate can be found in the supplementary Figures S1a–b.

The TO plate was generated by establishing an initial design domain that included six screws (three proximal and three distal), which was determined based on the results of comparing various screw configurations (*i.e.,* P3-D3 in Fig. 4a). The design domain was defined with a maximum thickness of 8.0 mm distally and 18.0 mm proximally, and a portion of the medial side was subtracted from the bone surface to achieve a good fit with the femur (Fig. 1c-i–ii and S1c of the supplementary document). The design area was 115.0 mm in length and 25.0 mm in width to cover the entire lateral side of the shaft (Figure S1c of the supplementary document). A total of 29 cycles of iterative general TO were performed using the TOSCA module within the Abaqus/CAE. We used the solid isotropic material with penalization (SIMP) method to describe how the density and stiffness of each element were related. The convergence criteria were set to 0.005 for element density changes and 0.001 for the objective function. The material distribution within the design domain was optimized for the extreme physiological loading condition (*i.e.,* walking) with the objective of minimizing the sum of strain energy while limiting the volume (the sum of the volumes of elements in the design area) to 30% of the design domain. The choice of a 30% volume constraint was made to find a balance between reducing material use and maintaining the integrity of the structure, while also avoiding potential convergence issues during the optimization process (Gupta et al., 2020). In addition to volume constraints, the model was

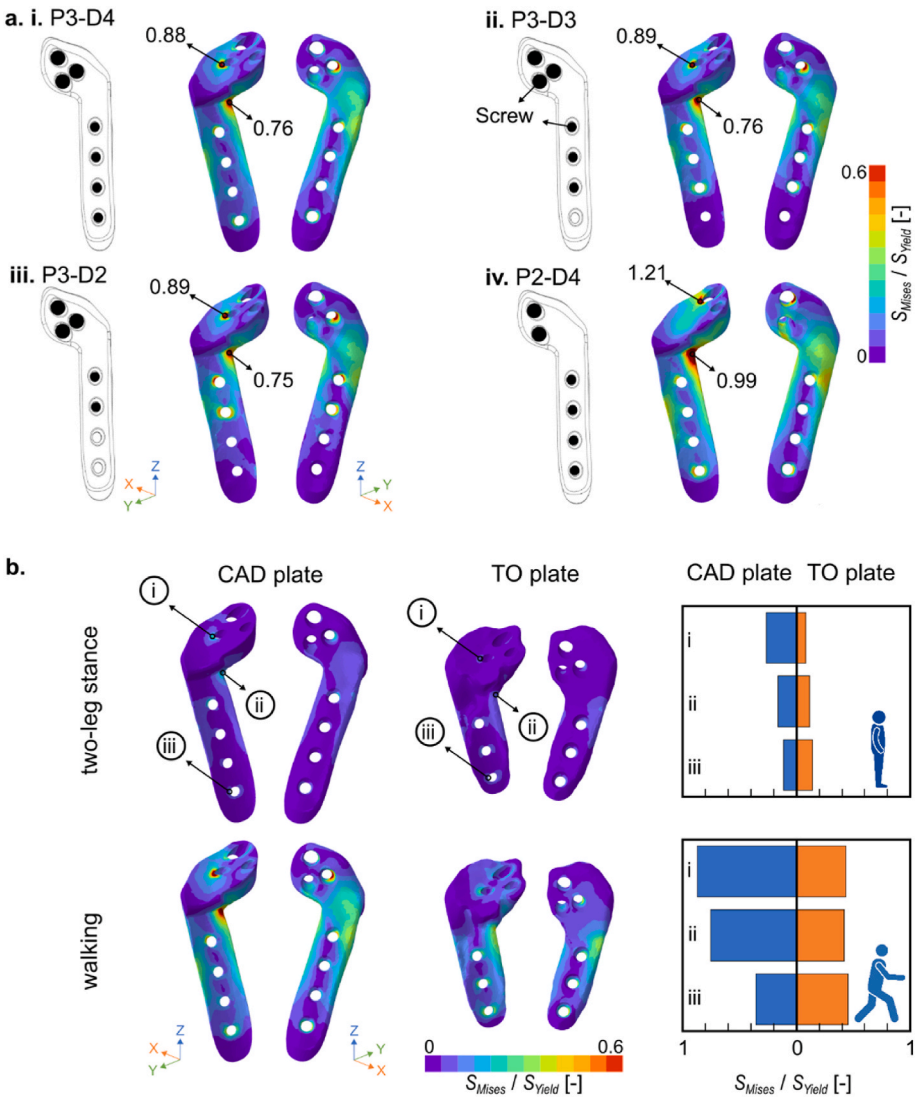

Fig. 4. (a) A comparative analysis of the FEA-predicted von Mises stress (S_{Mises}) distributions normalized by the yield strength (S_{Yield}) of the 3D-printed titanium alloy across varying screw configurations. These configurations include (i) three proximal screws and four distal screws (P3-D4), (ii) three proximal screws and three distal screws (P3-D3), (iii) three proximal screws and two distal screws (P3-D2), and (iv) two proximal screws and four distal screws (P2-D4). (b) A comparative evaluation of the FEA-predicted von Mises stress distributions (S_{Mises}/S_{Yield}) for both CAD and TO plates under two distinct conditions: two-leg stance and walking.

subjected to geometrical constraints. To ensure that there was sufficient material available for screw fixation, the area surrounding the screw holes was frozen and was, thus, excluded from TO. Since the overall shape of the plate was already determined, no extra geometric limitations were imposed during the optimization stage.

The resulting TO plate (Fig. 1c–iii) was then converted into a raw STL file using 3-matic® 13.0 (Materialise, Belgium) for post-processing. The raw STL file of the plate was imported and refined by removing any excess material and closing any openings that could potentially cause tissue integration, ensuring a solid plate structure. The edges were then rounded, and the final design was smoothed to minimize the risk of tissue irritation, friction between the plate and surrounding tissues, and bone ingrowth (Wang et al., 2017; Liu et al., 2014). The surface modifications were finalized after consultation with the orthopedic surgeon (Fig. 1c–iv).

2.5. Experimental methods

CAD and TO plates were additively manufactured from Ti–6Al–4V ELI powder (grade 23), and were fixed to the synthetic bone using standard Ti–6Al–4V cannulated dynamic compression screws (MatrixMANDIBLE, DePuy Synthes, USA). The plates were manufactured using the direct metal printing (DMP) technique using a layer thickness of 60 μm (3D systems, Leuven) and were post-processed through hot isostatic pressing (HIP) (105 MPa, 1050 °C, dwell time = 120 min). The chemical composition and mechanical properties of the used titanium alloy powder are listed in Tables S2 and S3 of the supplementary document, respectively.

The surgical cutting and drilling guide (Figure S1d of the supplementary document) was manufactured using the Formlabs surgical guide resin, which is a biocompatible photopolymer material specifically designed for use in surgical guide applications, and stereolithography (SLA) technique on a Form 3B printer (Formlabs, USA). The bone-plate construct was prepared in accordance with the virtual surgical plan by positioning the guide on the FDM 3D printed femur affected by SCFE. The screw holes were first predrilled with a 1.6-mm drill bit, and the wedge-shaped excess portion was removed using a hand saw. The plate was then screwed onto the proximal and distal femur sections with the aid of Kirschner wires inserted into the predrilled holes (Figure S1d of the supplementary document). During the screwing process, the applied torques were measured (Stahlwille Torque Screwdriver 760, Germany), and the maximum torque was set at 1.5 N m

(Kincaid et al., 2007; Yerby et al., 2001; Daftari et al., 1994).

The experimental test setup was devised to perform both quasi-static compression and cyclic testing (Fig. 2a). The setup comprised a fixture consisting of a cup-shaped top and a box-shaped bottom to simulate the interaction between the head of the femur and the joint. The bone, which was fixed in place using epoxy resin (Poly-Pox epoxy THV 500 and hardener Poly-Pox 355, Poly-Service), was positioned at the bottom part of the fixture and angled at 20° in the coronal plane to replicate physiological posture. The cup's diameter was set to 47.0 mm to fit the sphere-shaped femoral head and its depth was set at 15.0 mm to minimize the risk of impingement. The fixture was designed using SolidWorks (Dassault Systèmes SolidWorks Corp., V2020) and was fabricated through milling. To imitate physiological posture during the curing process, a holder was utilized to maintain the constructs at a 20° angle in the coronal plane (Figure S1e of the supplementary document).

2.5.1. Quasi-static compression testing protocol

We conducted quasi-static compression tests on two CAD and three TO constructs using a mechanical testing bench (LLOYD instrument LR5K with a 5000 N load cell) at a rate of 0.3 mm/min with a preload of 1.0 N until failure occurred. The failure of the construct was determined as plate, screw, or bone failure or as screw loosening. The stiffness of the construct was calculated using the slope of the best-fit line in the linear portion of the load-displacement curve, while the strain energy stored in the construct was calculated as the area under the curve until the failure.

2.5.2. Compression-compression cyclic testing protocol

Three CAD and three TO constructs were subjected to cyclic loading under a constant range of compressive stresses between 150 N and 1500 N (equivalent to 1.5 times BW) using an INSTRON ElectroPuls™ E10000 machine with a 10 KN load cell (Fig. 5a and b). To assess the long-term mechanical function of the plates, we evaluated them under a post-surgical worst-case loading condition within the first 150,000 cycles, which roughly corresponds to 15 min of walking with crutches per day for 5 months. To simulate this scenario, sinusoidal loads with 1 Hz oscillation were applied to the synthetic bone specimens for 150,000 cycles, based on physiological walking loading speeds and recovery times (Kanchanomai et al., 2010). If no plate or construct failure was observed after 150,000 cycles, the test was extended to 1,000,000 cycles at 3 Hz to detect any potential plate or screw failures (Fig. 5b).

2.5.3. DIC measurements

The local deformation and strain patterns during the experimental testing were measured using a Q-400 2 × 12 MPixel digital image correlation (DIC) system (LIMESS GmbH, Krefeld, Germany). The strain maps were obtained for both the CAD and TO plates at a frequency of 0.25 Hz and a facet size of 21–27 pixels. To study the full-field strain distribution of the bone plate, the plate itself was selected as the region of interest. A black dot speckle pattern was applied over a white paint background, covering the entire area of interest. Two digital cameras and LED panels were positioned at a distance of 0.8 m from the specimens to capture images and provide illumination, respectively. Image processing and strain calculations were performed using Istra4D x64 4.6.5 software (Dantec Dynamics A/S, Skovunde, Denmark). The logarithmic strain (LE) maps from FEA were then compared to the true principal strain maps measured with DIC within the linear region (Fig. 2b).

3. Results

3.1. FEA results

The computational model was validated by comparing the logarithmic (LE) maximum principal strain in the linear elastic range (up to 1700 N) as predicted by the FEA model with the maximum principal true strain measured using DIC (Fig. 2c). The comparison showed good agreement between the two, indicating that the FEA model is a valid representation of the experimentally obtained maximum principal strain fields. Both the DIC and FEA results revealed increased strain in the vicinity of the top screw in the shaft and towards the fracture gap at the lateral side of the CAD plate (Fig. 2c). The DIC results also showed high strain fields at the top of the plate, which were not captured in the FEA.

Although the CAD plate was marked with small holes for monitoring print quality, these holes were not included in the FE model. However,

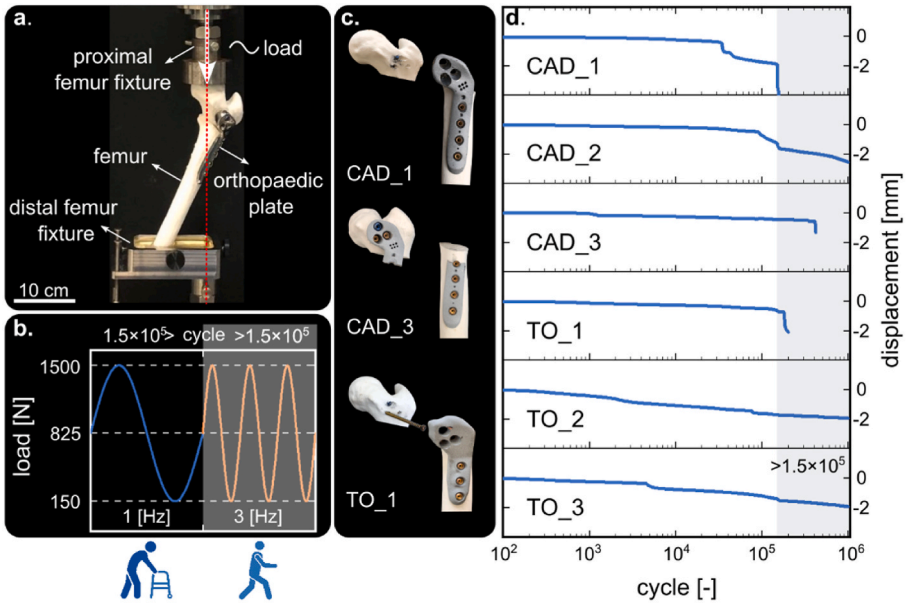

Fig. 5. The setup used for cyclic loading tests and the corresponding experimental results. (a) The setup used for the cyclic loading tests, (b) the cyclic compressive load changed between a minimum of 150 N and a maximum of 1500 N with an initial frequency of 1 Hz until 150,000 cycles. The specimens surviving the first round of the cyclic test were subjected to cyclic loading with the same maximum and minimum loads applied with a frequency of 3 Hz until a total of 1,000,000 cycles (including the first round of tests), and (c) the different modes of failure observed in this study. (d) The displacement *vs.* number of cycles for both CAD and TO plates during the cyclic tests.

the results of both experimental testing and FE analysis were found to be comparable, suggesting that these small holes did not significantly affect the performance of the plate.

The FEA model was expanded to assess the performance of orthopedic plates with various designs and screw configurations under physiological loading conditions. The von Mises stress distribution resulted from the FEA were compared in two-leg stance and walking conditions (Fig. 4b). Under both physiological loading conditions, the CAD plate showed the highest degrees of stresses concentration in the vicinity of the most lateral proximal screw, with maximum stress values of 233.0 MPa and 762.0 MPa ($S_{Mises}/S_{Yield} > 0.5$) in two-leg stance and walking, respectively (region i in Fig. 4b). In contrast, the TO plate exhibited a more homogeneous stress distribution within the safety margin ($S_{Mises}/S_{Yield} < 0.5$) (Fig. 4b-right). The CAD plate experienced higher stress concentration on the medial side near the fracture gap (region ii in Fig. 2b), exceeding the safety margin for walking conditions. This result suggests that if walking loads are applied, the stress on the medial side of the CAD plate could potentially lead to plate fractures.

The stress distributions in the analyzed screw configurations were comparable with a variation of less than 5% in the maximum stress between configurations P3-D4, P3-D3, and P3-D2 (Fig. 4a). However, a higher concentration of stress was noticed in the screw configuration P3-D2 at its most distal screw, resulting in a larger high stress area. The presence of fewer screws in the proximal part of the plate (*i.e.*, P2-D4) resulted in a significantly higher maximum von Mises stress, with a difference of 36% ($\sim$ 1055.0 MPa). All the configurations resulted in stress concentrations above the safety margin of 435 MPa in the plate. The configuration P3-D3 was ultimately selected for the topology optimization process.

The length of the TO plate was reduced by 18.1% in comparison to the CAD plate. The maximum thickness around the fracture gap, however, was increased by $\sim$ 30%, and the lateral side of the distal plate was doubled (Figure S1 of the supplementary document). The final plate had a maximum length of 86.0 mm, a variable width of around 20.0 mm and a variable thickness ranging from 4.0 to 8.0 mm distally (Figure S1c of the supplementary document). The TO plate weighed 62.6 g, which was 23.1% heavier (50.86 g) than the CAD plate. During two-leg stance loading, the maximum von Mises stress was recorded at 121.1 MPa near the bottom screw in the shaft. Walking loading resulted in a maximum von Mises stress of 390.7 MPa at the same location as observed in two-leg stance loading (Fig. 4b). High stress areas were observed in the bone near the interface between both bone parts, with maximum stress values of 96.1 and 147.0 MPa for two-leg stance and walking, respectively. The von Mises stresses inside the plate remained below the yield strength of Ti–6Al–4V (*i.e.,* 870 MPa).

3.2. Experimental test results

As a part of this study, unpublished data was used to evaluate the impact of screw torque measurements on the results. Two scenarios were examined: fully tightened screwing and screwing with a maximum torque of 1.5 N.m. The findings indicated that including screw torque measurements significantly enhances the consistency of the results. Without torque measurement, the outcomes were found to be highly variable. Consequently, all the results presented in this study were obtained from the construct tightened to a maximum torque of 1.5 N.m. The force-displacement data was obtained from quasi-static compression tests until failure (Fig. 2b). All the CAD constructs failed at loads lower than the maximum walking load of 3000 N (2814.4 $\pm$ 228.6 N), whereas all the three TO constructs failed at loads higher than the walking loading condition (>3000 N) at 3603.3 $\pm$ 108.2 N.

The mean stiffness of the CAD and TO constructs was determined to have a difference of 11.7%. However, a discrepancy was observed between the experimental results and those obtained using FEA, with the CAD and TO constructs exhibiting a 14.76% and 4.9% difference, respectively. The results of the quasi-static test indicated that the ultimate load values for the TO constructs were significantly higher (*i.e.*, 24.6%) as compared to those for the CAD constructs. The ultimate displacement and stored strain energy in the TO plates were observed to be greater than those in the CAD plates with increase of 34.6% and 78.1%, respectively. This data substantiates the enhanced capability of the TO plates to sustain higher levels of deformation and absorb more energy.

The true effective (von Mises) strain fields of the plates were obtained from the DIC measurements before the plates failed (Fig. 2b). In the CAD plate, the highest strain values were located near the fracture gap and the first distal screw due to bending moments. Conversely, the highest strain values in the TO plate were found in the proximal part of the plate, near the lateral screw hole. The CAD and TO constructs failed as a result of excessive bending, which led to the breakage of the lateral proximal screw. Bending was also visible at the remaining proximal screws in both the CAD and TO constructs and at the most distal screw in the shaft in two TO constructs (Fig. 2b). Neither the CAD nor the topology-optimized Ti–6Al–4V plates experienced plate failure.

In this study, the failures observed during the cyclic tests were categorized as screw failure, bending, or loosening, or as plate failure. Out of the three CAD constructs, two failed within 150,000 cycles, due to screw failure (*i.e.,* CAD_1 in Fig. 5c and d) and screw bending (*i.e.,* CAD_2). All of the topologically optimized constructs, on the other hand, were able to withstand cyclic loading within the same timeframe. When the tests were continued until 1,000,000 cycles, CAD_3 failed at the most proximal screw hole in the shaft after 400,000 cycles, while TO_1 failed at the two most proximal screws after 180,000 cycles (Fig. 5c). The other two TO constructs remained functional with slight displacement changes (<2 mm) until the end of the 1,000,000 cycles. During the removal of the plates, no screws were found to be loose.

4. Discussion

We evaluated the biomechanical performance of patient-specific fixation plates designed using two different design strategies (*i.e.*, CAD and TO) used for temporary fixation of bones following osteotomy. An FE model was created, validated against experimental results including full-field strain measurements, and used to examine the behavior of these plates under clinically relevant loading scenarios.

While PLA does not entirely mimic the mechanical properties of cortical bone tissue, it does possess characteristics resembling those of cancellous bone (Wu et al., 2020). Moreover, when comparing different design alternatives, the ranking of different designs in terms of their mechanical performance is not expected to be as much influenced by the absolute values of the mechanical properties of the bone phantom as it is by any inconsistencies (variabilities) in the geometry or mechanical properties of the bone phantom. Utilizing PLA offers a homogeneous, bone-like 3D-printed structure with consistent mechanical properties and patient-specific geometry, which allows for a methodical assessment of the effectiveness of patient-specific metallic bone plates. This standardized setup facilitates the comparison of different plate designs under consistent conditions. The test results demonstrated that there was no occurrence of screw loosening or bone failure. Given that the synthetic bone used here has a lower strength than actual cortical bone, the results of the current study suggest that the bone-plate constructs are not expected to experience failure if real bone is used (Egol et al., 2004). Although the findings are not directly translatable to clinical settings, previous research has established that the use of composite bone is a viable method for evaluating bone-plate constructs (MacLeod et al., 2018; Elfar et al., 2014).

The TO plate was designed with a smaller design area and a specific screw configuration that consisted of three distal and three proximal screws. The shape of the TO plate was similar to the CAD plate, but it was 20 mm shorter and thicker, with a maximum thickness of 8.0 mm distally and 18.0 mm proximally, compared to 4.0 mm and 14.0 mm in the CAD plate, respectively. The use of three distal screws, instead of the

four used in the CAD plate, will likely reduce surgical incision size, surgery time while improving the patient recovery post-surgery (Nobari et al., 2010; Peleg et al., 2006; Petersik et al., 2018). The reduction in plate length also allows for better adaptation to the specific anatomy of the patient, enhancing the fit and reducing potential issues related to plate positioning. The increased thickness around the fracture gap helps to provide better stability and increase load-bearing capacity and support, particularly in areas where bending forces may be more prominent. This reinforcement helps to distribute the load more effectively and prevent stress concentrations, reducing the risk of plate failure. Although previous studies have shown that reducing the plate length and increasing its thickness can result in increased plate stiffness (Stoffel et al., 2003; Petersik et al., 2018; Chakladar et al., 2016), these effects were minimal in the bone-plate constructs studied here. The stiffness of the construct differed by only 11.7% between the CAD and TO plates, with the TO construct displaying higher values of ultimate load, ultimate displacement, and stored strain energy as compared to the CAD construct.

The TO plate was 23.1% heavier than the CAD plate. The increased weight of the TO plate, although it may not be desirable in terms of implant weight, can contribute to improved stability and load distribution. A heavier plate can provide additional rigidity and resistance against deformations under load. After consultation with the surgeon, the extra weight was deemed acceptable.

We conducted a computational evaluation of the plates under simulated physiological loading conditions. Our results indicated that during walking and in the case of the CAD plate, the stress values within the areas of stress concentration exceeded the yield limit of 435 MPa ($S_{Mises}/S_{Yield} > 0.5$), while the TO plate remained below this limit in both two-leg stance and walking scenarios. This suggests that the CAD plate is at increased risk of failure, potentially leading to plastic deformation or crack initiation (Caiti et al., 2019), when subjected to a load of ≈3000 N. The computational findings are supported by the experimental results, including the cyclic and quasi-static loading tests, in which all the CAD constructs failed before reaching 3000 N.

The loading conditions applied to the hip joint were simplified in an effort to emulate the physiological loading conditions. Previous research has taken various approaches in representing the forces acting on the hip joint, including the inclusion of all muscles, only the primary muscles and joint forces, or just the hip contact force (Fan et al., 2018). The distribution of stress and strain around the bone and plate can vary depending on the loading conditions used (Fan et al., 2018; Taylor et al., 1996). Some studies have reported that including all the muscles in the hip joint leads to a more uniform distribution of strain along the femur (Duda et al., 1998), while others have found that only including the main muscles, such as the abductor and iliotibial tract, can cause increased strains at the distal part of the bone (Duda et al., 1997). It is important to consider the contribution of muscle forces in FEA models, as neglecting them can lead to an overestimation of shear and bending forces (Duda et al., 1997, 1998). Including certain muscles, such as the obturator internus, iliopsoas, and superior and inferior gemellus, can help in decreasing the modeling errors (Duda et al., 1997). However, in order to balance the complexity of the model with the accuracy of the results, it is necessary to make compromises and decisions about the inclusion of muscles in the FEA models. Further research is needed to better understand what impact these simplifications have on the simulation results.

The osteotomy procedure for patients with SCFE is intended to re-establish healthy loading conditions in the hip joint. It is, however, likely that these conditions remain weaker than normal after surgery due to reduced weight-bearing activities during the recovery period. In this study, forces generated by healthy muscles were used to analyze the forces acting on the femur, which may have resulted in an overestimation of these forces. This overestimation could have also been due to the simplified muscle model and the angle at which the muscle forces are applied (Bitsakos et al., 2005). Although the loading conditions used in this study may not precisely reflect the actual conditions encountered by the patient, the results of the plate strength analysis are likely still conservative, implying that the actual forces are probably lower than what was estimated. This offers a margin of safety, as the analysis results provide an indication of the minimum required strength for the plate to perform effectively.

The bone model was simplified by assuming isotropic linear elastic material properties, which is a commonly used assumption in biomechanical modelling of bones (Caiti et al., 2019; Yang et al., 2010), while the screws were modelled as fully constrained beam elements. Both the screws and the plate contribute to the deformation during the experiments. In the FEA model, however, the screws are considered rigid, causing the deformation from the screws to be transferred to the plate. This could result in higher strain values on the plate in the FEA as compared to the DIC measurements. In addition to the simplifications made in the FE model, this discrepancy may have been caused by the out-of-view motion of the plate towards the DIC camera. However, the stiffness values obtained from the force-displacement curves were found to be similar between the experiments and the FEA, which may be because this method compares the deformation of the entire construct rather than just the plate.

During the quasi-static compression tests, the load was applied only to the head of the femur, which may lead to an overestimation of load transfer, particularly with respect to bending in bone-plate constructs (Duda et al., 1997, 1998). Some studies have attempted to incorporate tension at the greater trochanter in their loading device (Kanchanomai et al., 2010; Cordey et al., 1999). However, this is a challenging task, and there are concerns that the synthetic bone 3D printed from PLA may fail at this location (Cordey et al., 1999). Despite these challenges, research has shown that acceptable results can still be obtained without incorporating more complex physiological loading conditions (Arnone et al., 2013; Cordey et al., 1999).

The results of this study showed that the screws, particularly those located proximally, were the weakest part of all the tested constructs. The proximal cannulated screws of 4.5 mm diameter failed due to bending moments, a common mode of failure in bone plate constructs (Stoffel et al., 2003). Bending was also observed in the other proximal screws in both plate constructs and in the most distal screw of the TO plate construct, which may be due to higher loads being applied to the TO plate construct prior to failure as compared to the CAD construct. To improve the performance of the constructs, it is suggested to consider increasing the diameter of the proximal screws and/or replacing cannulated screw with solid screws or other enhancements. In addition, this study highlighted the high variability in test results when screw torque was not measured. In our preliminary experimental tests, we observed that the torques applied to the screws can significantly influence the overall performance of the plates. Measuring screw torque resulted in more consistent outcomes. Moreover, excessive tightening torques have been identified in the literature as a major contributor to screw failure in bone plate constructs (Daftari et al., 1994). It is, therefore, recommended to take screw insertion torques into consideration during surgical procedures. Incorporating this variable in computational models could facilitate a parametric investigation of how varying torque levels applied to the screws affects the biomechanical performance of the plates. Such computational simulations can provide considerable added value particularly in surgical settings.

We also compared the performance of the CAD and TO plates under cyclic loading conditions. The results showed that the CAD plates are more likely to fail within 150,000 cycles of loading, due to screw bending and screw material failure. As cyclic loading continued (up to 1,000,000 cycles), the remaining CAD plate and one of the TO plates failed, while both other TO constructs performed well. The overall outcome indicated that the TO plates were more durable and more capable of withstanding cyclic loads as compared to the CAD plates. However, it is important to note that these findings are only applicable to the specific loading conditions tested and may not be generalizable to

other loading conditions. Moreover, the optimal design for a patient-specific plate may vary depending on various factors, such as bone anatomy, density, and osteotomy angle. Hence, further clinical testing is necessary to validate the strength of these plates in a clinical setting. The evaluation steps and finite element analysis used in this study can be applied in the design of patient-specific plates for SCFE patients. However, any design modifications should only be made after consulting with a qualified surgeon.

5. Conclusions

We present evidence that patient-specific bone plates designed using TO result in improved biomechanical performance, as demonstrated by higher ultimate loads and similar stiffness when compared to those designed using conventional CAD techniques. These results highlight the utility of TO as a valuable approach for designing custom bone plates for proximal femur fixation in patients with SCFE. The topology-optimized plates showed a more uniform stress distribution in the regions close to the screws, resulting in more durable constructs. While there were discrepancies between the results of the FEA models and experimental testing, the study showed that FEM data is a reliable tool for evaluating and optimizing bone plates for SCFE patients.

Ethical approval

The OLVG Hospital institutional review board granted permission for the anonymized CT dataset (WO20.057). The participant provided written consent to have his information used for research purposes.

CRediT authorship contribution statement

V. Moosabeiki: Conceptualization, Investigation, Formal analysis, Methodology, Visualization, Supervision, Writing – original draft. **N. de Winter:** Investigation, Formal analysis, Methodology, Visualization, Writing – review & editing. **M. Cruz Saldivar:** Investigation. **M.A. Leeflang:** Investigation, Methodology. **M.M.E.H. Witbreuk:** Conceptualization, Investigation, Formal analysis, Methodology, Resources, Supervision, Writing – review & editing. **V. Lagerburg:** Conceptualization, Investigation, Formal analysis, Methodology, Resources, Supervision, Writing – review & editing. **M.J. Mirzaali:** Conceptualization, Investigation, Formal analysis, Methodology, Supervision, Resources, Writing – review & editing. **A.A. Zadpoor:** Investigation, Formal analysis, Conceptualization, Supervision, Resources, Writing – review & editing, All authors have read and agreed to the published version of the manuscript.

Declaration of competing interest

The authors declare that they have no known competing financial interests or personal relationships that could have appeared to influence the work reported in this paper

Data availability

The data that has been used is confidential.

Appendix A. Supplementary data

Supplementary data to this article can be found online at https://doi.org/10.1016/j.jmbbm.2023.106173.

References

Al-Tamimi, A.A., Quental, C., Folgado, J., Peach, C., Bartolo, P., 2020. Stress analysis in a bone fracture fixed with topology-optimised plates. Biomech. Model. Mechanobiol. 19 (2), 693–699.

Anderson, I., 2017. Mechanical properties of specimens 3D printed with virgin and recycled polylactic acid. 3D Print. Addit. Manuf. 4 (2), 110–115.

Arnone, J.C., Sherif El-Gizawy, A., Crist, B.D., Della Rocca, G.J., Ward, C.V., 2013. Computer-aided engineering approach for parametric investigation of locked plating systems design. J. Med. Dev. Trans. ASME 7 (2).

Aronsson, D.D., Loder, R.T., Breur, G.J., Weinstein, S.L., 2006. Slipped capital femoral epiphysis: current concepts. JAAOS-J. Am. Acad. Orthop. Surg. 14 (12), 666–679.

Aziz, R., Haq, M.I.U., Raina, A., 2020. Effect of surface texturing on friction behaviour of 3D printed polylactic acid (PLA). Polym. Test. 85, 106434.

Bergmann, G., Bender, A., Dymke, J., Duda, G., Damm, P., 2016. Standardized loads acting in hip implants. PLoS One 11 (5), e0155612.

Bitsakos, C., Kerner, J., Fisher, I., Amis, A.A., 2005. The effect of muscle loading on the simulation of bone remodelling in the proximal femur. J. Biomech. 38 (1), 133–139.

Brouwer de Koning, S.G., de Winter, N., Moosabeiki, V., Mirzaali, M.J., Berenschot, A., Witbreuk, M.M.E.H., Lagerburg, V., 2023. Design considerations for patient-specific bone fixation plates: a literature review. Med. Biol. Eng. Comput. 1–20. Sep 11. https://doi.org/10.1007/s11517-023-02900-4.

Caiti, G., Dobbe, J.G., Bervoets, E., Beerens, M., Strackee, S.D., Strijkers, G.J., Streekstra, G.J., 2019. Biomechanical considerations in the design of patient-specific fixation plates for the distal radius. Med. Biol. Eng. Comput. 57 (5), 1099–1107.

Chakladar, N., Harper, L.T., Parsons, A., 2016. Optimisation of composite bone plates for ulnar transverse fractures. J. Mech. Behav. Biomed. Mater. 57, 334–346.

Cheal, E.J., Spector, M., Hayes, W.C., 1992. Role of loads and prosthesis material properties on the mechanics of the proximal femur after total hip arthroplasty. J. Orthop. Res. 10 (3), 405–422.

Chen, X., He, K., Chen, Z., 2017. A novel computer-aided approach for parametric investigation of custom design of fracture fixation plates. Comput. Math. Methods Med. 2017.

Chen, Y.-Y., Lin, K.-H., Huang, H.-K., Chang, H., Lee, S.-C., Huang, T.-W., 2018. The beneficial application of preoperative 3D printing for surgical stabilization of rib fractures. PLoS One 13 (10), e0204652.

Chung, C.-Y., 2018. A simplified application (APP) for the parametric design of screw-plate fixation of bone fractures. J. Mech. Behav. Biomed. Mater. 77, 642–648.

Ciarelli, M., Goldstein, S., Kuhn, J., Cody, D., Brown, M., 1991. Evaluation of orthogonal mechanical properties and density of human trabecular bone from the major metaphyseal regions with materials testing and computed tomography. J. Orthop. Res. 9 (5), 674–682.

Cordey, J., Borgeaud, M., Frankle, M., Harder, Y., Martinet, O., 1999. Loading model for the human femur taking the tension band effect of the ilio-tibial tract into account. Injury 30, SA26–SA30.

Cordey, J., Borgeaud, M., Perren, S., 2000. Force transfer between the plate and the bone: relative importance of the bending stiffness of the screws and the friction between plate and bone. Injury 31, 21–92.

Daftari, T.K., Horton, W.C., Hutton, W.C., 1994. Correlations between screw hole preparation, torque of insertion, and pullout strength for spinal screws. Clin. Spine Surg. 7 (2), 139–145.

Dobbe, J.G., Vroemen, J.C., Strackee, S.D., Streekstra, G.J., 2013. Patient-tailored plate for bone fixation and accurate 3D positioning in corrective osteotomy. Med. Biol. Eng. Comput. 51 (1), 19–27.

Duda, G.N., Schneider, E., Chao, E.Y., 1997. Internal forces and moments in the femur during walking. J. Biomech. 30 (9), 933–941.

Duda, G.N., Heller, M., Albinger, J., Schulz, O., Schneider, E., Claes, L., 1998. Influence of muscle forces on femoral strain distribution. J. Biomech. 31 (9), 841–846.

Egol, K.A., Kubiak, E.N., Fulkerson, E., Kummer, F.J., Koval, K.J., 2004. Biomechanics of locked plates and screws. J. Orthop. Trauma 18 (8), 488–493.

Elfar, J., Stanbury, S., Menorca, R.M.G., Reed, J.D., 2014. Composite bone models in orthopaedic surgery research and education. J. Am. Acad. Orthop. Surg. 22 (2), 111.

Erickson, J.B., Samora, W.P., Klingele, K.E., 2017. Treatment of chronic, stable slipped capital femoral epiphysis via surgical hip dislocation with combined osteochondroplasty and Imhauser osteotomy. J. Children's Orthopaed. 11 (4), 284–288.

Fan, X., Chen, Z., Jin, Z., Zhang, Q., Zhang, X., Peng, Y., 2018. Parametric study of patient-specific femoral locking plates based on a combined musculoskeletal multibody dynamics and finite element modeling. Proc. IME H J. Eng. Med. 232 (2), 114–126.

Farah, S., Anderson, D.G., Langer, R., 2016. Physical and mechanical properties of PLA, and their functions in widespread applications—a comprehensive review. Adv. Drug Deliv. Rev. 107, 367–392.

Von Fraunhofer, J., Schaper, L., Seligson, D., 1985. The rotational friction characteristics of human long bones. Surf. Technol. 25 (4), 377–383.

Gupta, D.K., van Keulen, F., Langelaar, M., 2020. Design and analysis adaptivity in multiresolution topology optimization. Int. J. Numer. Methods Eng. 121 (3), 450–476.

Gutwald, R., Jaeger, R., Lambers, F.M., 2017. Customized mandibular reconstruction plates improve mechanical performance in a mandibular reconstruction model. Comput. Methods Biomech. Biomed. Eng. 20 (4), 426–435.

Henderson, C.E., Kuhl, L.L., Fitzpatrick, D.C., Marsh, J., 2011. Locking plates for distal femur fractures: is there a problem with fracture healing? J. Orthop. Trauma 25, S8–S14.

Herngren, B., Stenmarker, M., Vavruch, L., Hagglund, G., 2017. Slipped capital femoral epiphysis: a population-based study. BMC Muscoskel. Disord. 18 (1), 1–12.

Kanchanomai, C., Muanjan, P., Phiphobmongkol, V., 2010. Stiffness and endurance of a locking compression plate fixed on fractured femur. J. Appl. Biomech. 26 (1), 10–16.

Kincaid, B., Schroder, L., Mason, J., 2007. Measurement of orthopedic cortical bone screw insertion performance in cadaver bone and model materials. Exp. Mech. 47 (5), 595–607.

Kobryn, P., Semiatin, S., 2001. Mechanical Properties of Laser-Deposited Ti-6Al-4V, 2001 International Solid Freeform Fabrication Symposium.
Van Kootwijk, A., Moosabeiki, V., Saldivar, M.C., Pahlavani, H., Leeflang, M., Niar, S.K., Pellikaan, P., Jonker, B., Ahmadi, S., Wolvius, E., 2022. Semi-automated digital workflow to design and evaluate patient-specific mandibular reconstruction implants. J. Mech. Behav. Biomed. Mater. 132, 105291.
van Kootwijk, A., Jonker, B.P., Wolvius, E.B., Saldivar, M.C., Leeflang, M.A., Zhou, J., Tümer, N., Mirzaali, M.J., Zadpoor, A.A., 2023. Biomechanical evaluation of additively manufactured patient-specific mandibular cage implants designed with a semi-automated workflow: a cadaveric and retrospective case study. J. Mech. Behav. Biomed. Mater. 146, 106097.
Liu, P.-c., Yang, Y.-j., Liu, R., Shu, H.-x., Gong, J.-p., Yang, Y., Sun, Q., Wu, X., Cai, M., 2014. A study on the mechanical characteristics of the EBM-printed Ti-6Al-4V LCP plates in vitro. J. Orthop. Surg. Res. 9.
Loder, R.T., Aronsson, D.D., Dobbs, M.B., Weinstein, S.L., 2000. Slipped capital femoral epiphysis. JBJS 82 (8), 1170.
Ma, L., Zhou, Y., Zhu, Y., Lin, Z., Chen, L., Zhang, Y., Xia, H., Mao, C., 2017. 3D printed personalized titanium plates improve clinical outcome in microwave ablation of bone tumors around the knee. Sci. Rep. 7 (1), 1–10.
MacLeod, A., Serrancoli, G., Fregly, B.J., Toms, A., Gill, H., 2018. The effect of plate design, bridging span, and fracture healing on the performance of high tibial osteotomy plates: an experimental and finite element study. Bone & Joint Res. 7 (12), 639–649.
Manoff, E.M., Banffy, M.B., Winell, J.J., 2005. Relationship between body mass index and slipped capital femoral epiphysis. J. Pediatr. Orthop. 25 (6).
Mirzaali, M., Bobbert, F., Li, Y., Zadpoor, A., 2019. Of metals using powder bed-based technologies. Addit. Manuf. 93.
Mirzaali, M.J., Azarniya, A., Sovizi, S., Zhou, J., Zadpoor, A.A., 2021. 16 - lattice structures made by laser powder bed fusion. In: Yadroitsev, I., Yadroitsava, I., du Plessis, A., MacDonald, E. (Eds.), Fundamentals of Laser Powder Bed Fusion of Metals. Elsevier, pp. 423–465.
Mirzaali, M.J., Moosabeiki, V., Rajaai, S.M., Zhou, J., Zadpoor, A.A., 2022. Additive manufacturing of biomaterials—design principles and their implementation. Materials.
Mirzaali, M.J., Shahriari, N., Zhou, J., Zadpoor, A.A., 2023. Chapter Sixteen - quality of AM implants in biomedical application. In: Kadkhodapour, J., Schmauder, S., Sajadi, F. (Eds.), Quality Analysis of Additively Manufactured Metals. Elsevier, pp. 689–743.
Nobari, S., Katoozian, H., Zomorodimoghadam, S., 2010. Three-dimensional design optimisation of patient-specific femoral plates as a means of bone remodelling reduction. Comput. Methods Biomech. Biomed. Eng. 13 (6), 819–827.
Novais, E.N., Millis, M.B., 2012. Slipped capital femoral epiphysis: prevalence, pathogenesis, and natural history. Clin. Orthop. Relat. Res. 470 (12), 3432–3438.
Peleg, E., Mosheiff, R., Liebergall, M., Mattan, Y., 2006. A short plate compression screw with diagonal bolts—a biomechanical evaluation performed experimentally and by numerical computation. Clin. BioMech. 21 (9), 963–968.
Pendergast, M., Rusovici, R., 2015. A finite element parametric study of clavicle fixation plates. Int. J. Num. Method. Biomed. Eng. 31 (6), e02710.
Perry, D.C., Metcalfe, D., Lane, S., Turner, S., 2018. Childhood obesity and slipped capital femoral epiphysis. Pediatrics 142 (5).
Petersik, A., Homeier, A., Hoare, S.G., von Oldenburg, G., Gottschling, H., Schröder, M., Burgkart, R., 2018. A numeric approach for anatomic plate design. Injury 49, S96–S101.
Reina-Romo, E., Giráldez-Sánchez, M., Mora-Macías, J., Cano-Luis, P., Domínguez, J., 2014. Biomechanical design of Less Invasive Stabilization System femoral plates: computational evaluation of the fracture environment. Proc. IME H J. Eng. Med. 228 (10), 1043–1052.
Sathish, T., Kumar, S.D., Muthukumar, K., Karthick, S., 2020. Temperature distribution analysis on diffusion bonded joints of Ti-6Al-4V with AISI 4140 medium carbon steel. Mater. Today: Proc. 21, 847–856.
Shibahara, T., Noma, H., Furuya, Y., Takaki, R., 2002. Fracture of mandibular reconstruction plates used after tumor resection. J. Oral Maxillofac. Surg. 60 (2), 182–185.
Shockey, J., Von Fraunhofer, J., Seligson, D., 1985. A measurement of the coefficient of static friction of human long bones. Surf. Technol. 25 (2), 167–173.
Simoes, J., Vaz, M., Blatcher, S., Taylor, M., 2000. Influence of head constraint and muscle forces on the strain distribution within the intact femur. Med. Eng. Phys. 22 (7), 453–459.
Soni, A., Singh, B., 2020. Design and analysis of customized fixation plate for femoral shaft. Indian J. Orthop. 54 (2), 148–155.
Stoffel, K., Dieter, U., Stachowiak, G., Gächter, A., Kuster, M.S., 2003. Biomechanical testing of the LCP–how can stability in locked internal fixators be controlled? Injury 34, B11–B19.
Taylor, M., Tanner, K., Freeman, M., Yettram, A., 1996. Stress and strain distribution within the intact femur: compression or bending? Med. Eng. Phys. 18 (2), 122–131.
Tilton, M., Armstrong, A., Sanville, J., Chin, M., Hast, M.W., Lewis, G.S., Manogharan, G. P., 2020. Biomechanical testing of additive manufactured proximal humerus fracture fixation plates. Ann. Biomed. Eng. 48 (1), 463–476.
Wang, D., Wang, Y., Wu, S., Lin, H., Yang, Y., Fan, S., Gu, C., Wang, J., Song, C., 2017. Customized a Ti6Al4V bone plate for complex pelvic fracture by selective laser melting. Materials 10 (1), 35.
Witbreuk, M.M.E.H., Bolkenbaas, M., Mullender, M.G., Sierevelt, I.N., Besselaar, P.P., 2009. The results of downgrading moderate and severe slipped capital femoral epiphysis by an early Imhauser femur osteotomy. J. Children's Orthopaed. 3 (5), 405–410.
Wu, D., Spanou, A., Diez-Escudero, A., Persson, C., 2020. 3D-printed PLA/HA composite structures as synthetic trabecular bone: a feasibility study using fused deposition modeling. J. Mech. Behav. Biomed. Mater. 103, 103608.
Wu, N., Li, S., Zhang, B., Wang, C., Chen, B., Han, Q., Wang, J., 2021. The advances of topology optimization techniques in orthopedic implants: a review. Med. Biol. Eng. Comput. 59 (9), 1673–1689.
Wylie, J.D., Novais, E.N., 2019. Evolving understanding of and treatment approaches to slipped capital femoral epiphysis. Curr. Rev. Musculoskeletal Med. 12 (2), 213–219.
Yang, H., Ma, X., Guo, T., 2010. Some factors that affect the comparison between isotropic and orthotropic inhomogeneous finite element material models of femur. Med. Eng. Phys. 32 (6), 553–560.
Yang, P., Lin, T.-Y., Xu, J.-L., Zeng, H.-Y., Chen, D., Xiong, B.-L., Pang, F.-X., Chen, Z.-Q., He, W., Wei, Q.-S., 2020. Finite element modeling of proximal femur with quantifiable weight-bearing area in standing position. J. Orthop. Surg. Res. 15 (1), 1–10.
Yerby, S., Scott, C.C., Evans, N.J., Messing, K.L., Carter, D.R., 2001. Effect of cutting flute design on cortical bone screw insertion torque and pullout strength. J. Orthop. Trauma 15 (3), 216–221.
Yu, H., Cai, Z., Zhou, Z., Zhu, M., 2005. Fretting behavior of cortical bone against titanium and its alloy. Wear 259 (7–12), 910–918.
Zadpoor, A.A., 2017. Design for additive bio-manufacturing: from patient-specific medical devices to rationally designed meta-biomaterials. Int. J. Mol. Sci. 18 (8), 1607.
Zhiani Hervan, S., Altınkaynak, A., Parlar, Z., 2021. Hardness, friction and wear characteristics of 3D-printed PLA polymer. Proc. IME J. J. Eng. Tribol. 235 (8), 1590–1598.